Acta Mechanica 120, 91–107 (1997)

ACTA MECHANICA

Uni-axial strain loading of a rubber rod by planar shock waves

O. Igra, L. Wang, and **G. Ben-Dor,** Beer Sheva, Israel, and **H. Reichenbach** and **W. Heilig,** Freiburg, Germany

(Received June 30, 1995; revised November 15, 1995)

Summary. The uni-axial strain loading of a rubber rod struck head-on by a planar shock wave is studied experimentally and numerically. A physical model capable of describing the rubber response to its collision with the incident shock wave is proposed. This model takes into account the rubber compressibility and the friction forces developed in the contact surface between the rubber and its surrounding rigid walls. The good agreement that exists between experiments and their numerical simulations verifies the validity of the proposed physical model and the accuracy of the numerical scheme used for the numerical simulations. It is found that for the considered loading mode, i.e., uni-axial strain loading, no shock waves exists in the rubber rod. The stresses measured/calculated in the rod result from compression wave motion (with constant velocity) in it. It is also found that the friction developed between the rubber rod and its bordering rigid walls plays an important role in damping the intensity of the wave propagating in the rubber due to its collision with the incident shock wave. The larger is the friction, the larger is the stress damping rate in the rubber.

1 Introduction

Head-on reflection of shock waves from a rigid, stationary wall is well known and documented [1], [2]. In such cases, the head-on reflection phenomenon is characterized by a zero flow velocity behind the reflected shock wave. In nature, however, head-on reflection of normal shock waves from non-rigid boundaries can occur. Cases in which one finds shock wave reflection from, and propagation into, a non-rigid medium appear in many engineering problems. Some examples are: reflection of blast waves from rubber-coated bodies that can be found on a battle ground; shock-wave reflection from and penetration into live-tissue such as the case of lithotherapy; and the interaction of shock waves with foams used for pressure amplification. It is therefore of interest to understand better the head-on collision of planar shock waves with such boundaries. A detailed derivation of a physical model capable of describing shock wave reflection from and propagation into a rubber rod was given recently in Mazor et al. [3]. In this paper three different modes for the rubber loading by the incident shock wave are studied, namely,

(a) Uni-axial stress compression. The rubber-rod movement is limited only at its rear end, along the x-axis, where it is attached to a rigid boundary. The rubber is free to expand along the y- and z-axes, and its leading surface is free to move along the x-axis (see Fig. 1a). In this case $\sigma_y = \sigma_z = 0$ and $\varepsilon_y = \varepsilon_z \neq 0$.

(b) Bi-axial stress compression. The rubber-rod movements are limited at its rear surface, along the x-axis, as well as along the y-axis (due to its attachment to rigid boundaries at these locations, see Fig. 1b). The rubber is free to expand along the z-axis and its leading surface can move along the x-axis. In this case $\sigma_z = 0$ and $\varepsilon_y = 0$.

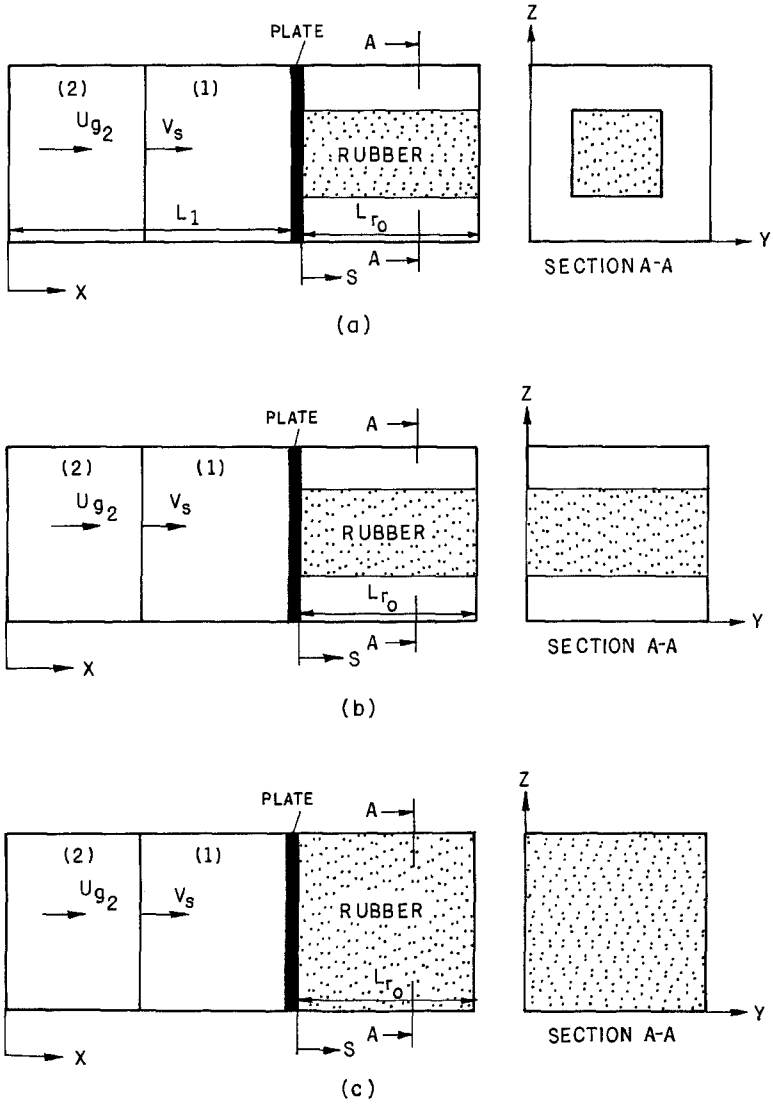

Fig. 1. Illustration of three different modes for applying a shock wave-induced compressive load: **a** uni-axial stress loading, **b** bi-axial stress loading, **c** uni-axial strain loading

(c) Uni-axial strain compression. The rubber rod movements along the y- and z-axes and its rear surface movement along the x-axis are limited by rigid walls (see Fig. 1c). Therefore, excluding its rear surface, it can move only along the x-axis. In this case $\varepsilon_y = \varepsilon_z = 0$ yand σ_x, σ_y and $\sigma_z \neq 0$.

A detailed derivation of the conservation and complementary equations describing the wave propagation and flow properties in the gas and in the rubber are given in Mazor et al. [3]. These equations are set up assuming that the rubber is incompressible and there is no friction between the rubber peripheral surfaces and the shock tube walls. While these assumptions are perfectly valid for the case of a uni-axial stress loading, and are reasonable for the case of a bi-axial stress loading (when lubricant is added between the rubber rod and the shock tube windows), they are highly questionable for the case of a uni-axial strain loading. In Mazor et al. [3] a comparison between experimental results and numerical simulations is made only for the bi-axial stress

loading case. It is therefore the purpose of the present paper to extend the physical model and its numerical solutions to cover the case of a uni-axial strain compression. The proposed physical model includes both the rubber compressibility and friction effects, since they play an important role during the rubber loading by the incident shock wave and its response to this loading.

2 Theoretical background

Assuming that the gaseous phase is an inviscid and thermally non-conductive ideal gas, i.e., its equation of state is $P = \varrho RT$ and its internal energy is given by $e = C_v T$, Mazor et al. [3] write the conservation equations for the gaseous and the solid phases using Lagrangian approach (see Eqs. (39) to (48) in their paper). In developing the governing equations for the solid phase (rubber) they assume that:

(a) The rubber is an isotropic elastic medium and changes in its internal energy are negligibly small.

(b) Body forces (gravity) and friction forces acting on the external surfaces of the rubber rod are negligibly small.

(c) Stresses developed in the rubber rod are uniformly distributed along any cross-sectional area perpendicular to the x-axis so that the rubber's cross-sectional area remains planar throughout the deformation process.

(d) The rubber is assumed to be incompressible.

For the present case, i.e., a uni-axial strain loading (see Fig. 1 c) assumptions (b) and (d) are unacceptable. Therefore, one must include friction forces and the rubber compressibility in the conservation equations. The only two equations to be effected by relaxing these two, unrealistic, assumptions are Eqs. (44) and (47) in [3]. Accounting for the rubber compressibility alters Eq. (44) in [3] to

$$\frac{\partial}{\partial t}\left[\varrho_r(h_r, t)\,\frac{\partial S(h_r, t)}{\partial h_r}\,A_r(h_r, t)\right] = 0. \tag{2.1}$$

Accounting for friction in the development of the conservation equations is manifested in one modification only: Consider a rubber rod element having a rectangular cross section of H by W, where H is its height and W is its width. The friction force exerted on its peripheral surfaces by the shock tube walls is

$$F_{\text{friction}} = 2(H + W)\,\Delta S \mu \sigma_n \operatorname{sign}(U_r) = \left[\frac{\Gamma_r}{A_r}\,\mu\,\frac{\nu}{1-\nu}\,\sigma_x \operatorname{sign}(U_r)\right] A_r \Delta S, \tag{2.2}$$

where ΔS, $\Gamma_r = 2(H + W)$, and $A_r = HW$ are elemental axial length, perimeter, and cross-sectional area of the element, respectively, μ and ν are the friction coefficient and the Poisson ratio, respectively. σ_n is the normal stress acting on the element surfaces; in the present case, $\sigma_n = \sigma_y$, and Eq. (35) in [3] is used for its evaluation. Defining a frictional force per unit volume as

$$\sigma_f = \frac{\Gamma_r}{A_r}\,\mu\,\frac{\nu}{1-\nu}\,\sigma_x \operatorname{sign}(U_r), \tag{2.3}$$

then, the rubber conservation of momentum, Eq. (47) in [3], is replaced by

$$\frac{\partial U_r}{\partial t} = -A_{r_0}\frac{\partial \sigma_x}{\partial h_r} - \frac{\sigma_f}{\varrho_r}. \tag{2.4}$$

In Eqs. (2.2) and (2.3) the function sign (x) is the sign operator which can take on values of $+1$ or -1 depending upon the sign of the argument x. It should be noted that unlike Eqs. (39) to (48) in [3], which are expressed in a nondimensional form, Eqs. (2.1) through (2.4) are expressed in a dimensional form.

3 The numerical scheme

For the numerical solution, the conservation equations were transformed to finite difference equations. In order to handle discontinuities, like shock waves, the artificial viscosity concept is used. Implementation of this concept effects equations describing conservation of momentum and energy in the gaseous phase and conservation of momentum in the rubber; therefore these equations are written as follows:
The equation of conservation of momentum for the gaseous phase reads

$$\frac{\partial U_g}{\partial t} = -\frac{\partial}{\partial h_g}(P_g + q_g), \tag{3.1}$$

and the equation of conservation of energy in the gaseous phase takes the form

$$C_v\frac{\partial T_g}{\partial t} = -[P_g + q_g]\frac{\partial V_g}{\partial t}, \tag{3.2}$$

where the artificial viscosity pressure term q_g includes both linear (see Landschoff [4]) and quadratic (see von Neumann and Richtmeyer [5]) terms; it is added only to compressed material elements. Specifically

$$q_g = q_L + q_N = -a_L \Delta x \varrho_g c\frac{\partial U_g}{\partial x} + a_N{}^2 \Delta x^2 \varrho_g \left(\frac{\partial U_g}{\partial x}\right)^2, \quad \text{for } \frac{\partial U_g}{\partial x} < 0,$$

that is

$$q_g = -\Delta x \varrho_g \frac{\partial U_g}{\partial x}\left[a_L c - a_N{}^2 \Delta x \frac{\partial U_g}{\partial x}\right]. \tag{3.3}$$

From mass conservation in the gaseous phase and the definition of the gas velocity, one obtains $\partial U_g/\partial x = 1/V_g\, dV_g/dt$. This leads to the following expression for the gaseous phase:

$$q_g = -\Delta h_g \frac{1}{V_g}\frac{dV_g}{dt}\left[a_L c - a_N{}^2 \frac{\Delta x}{V_g}\frac{dV_g}{dt}\right], \tag{3.4}$$

where c is the local speed of sound and $\Delta h_g = \varrho_g \Delta x$, a_L and a_N are constants (here $a_L = 0.6$ and $a_N = 1.5$).

It should be noted that Eq. (3.1) is written for a unit cross-section area and therefore A_g is dropped. The same is done, subsequently, for the rubber conservation of momentum. Writing the partial differential equation describing conservation of momentum in the gaseous phase in

a central finite difference form results in the following discretized expression:

$$(U_g)_i^{n+1} = (U_g)_i^n - \frac{\Delta t}{\Delta h_g}\left[(P_g)_{i+1/2}^n + (q_g)_{i+1/2}^n - (P_g)_{i-1/2}^n - (q_g)_{i-1/2}^n\right]. \tag{3.5}$$

The gas pressure P can be expressed in terms of temperature T and specific volume V using the equation of state for an ideal gas. When this is inserted in Eq. (3.2) the following semi-implicit discretized form for the gas energy equation is obtained:

$$(T_g)_{i+1/2}^{n+1} = \frac{\left(1 - \dfrac{(\gamma-1)}{2V_g^n}\Delta V_g\right) T_g^n - \dfrac{q_g}{C_v}\Delta V_g}{1 + \dfrac{(\gamma-1)}{2V_g^{n+1}}\Delta V_g}, \tag{3.6}$$

where $\Delta V_g = V_g^{n+1} - V_g^n$ and γ is the gas specific heat ratio.

The conservation of momentum for the rubber, Eq. (2.4), should be replaced by

$$\frac{\partial U_r}{\partial t} = -\frac{\partial}{\partial h_r}\left[\sigma_x(h_r, t) + q_r\right] - \frac{\sigma_f}{\varrho_r}, \tag{3.7}$$

where the artificial viscosity pressure term for rubber, q_r, is similar to that of the gas (see Eq. (3.3)). The discretized form of Eq. (3.7) is similar to that of the gas. The conservation of mass is satisfied automatically in the present Lagrangian method.

For calculating the movement of the interface separating the gas and the rubber a mixed element is used; half gas and half rubber. The momentum equation for the mixed element, in discretized form, is

$$\left(\frac{\Delta h_g}{2} + \frac{\Delta h_r}{2}\right)\frac{\Delta U_f}{\Delta t} = -\left[(\sigma_x + q_r)_{i+1/2}^n - (p_g + q_g)_{i-1/2}^n + \sigma_f \frac{\Delta S}{2}\right], \tag{3.8}$$

where U_f is the interface velocity.

4 Results and discussion

Experiments were conducted in the shock tube of the Ernst Mach Institute, Freiburg, Germany. This shock tube has an inner diameter of 20 cm. The driver section is 180 cm long, the driven section is 888 cm long, and the test section is located about 721 cm downstream of the diaphragm. A schematic description of this tube is shown in Fig. 2. Cellulose acetate sheets were used as diaphragms for separating between the two sections. This was proven to be an excellent diaphragm material, since it is brittle when stretched and has a high breaking velocity. The shock tube has a test section equipped with plane, parallel windows of high optical quality glass. The optical field of view is 200 mm × 110 mm and its depth is 40 mm. It is designed for using 'two-dimensional' models. During experiments the gas flow and the rubber behaviour were monitored by pressure measurements using Kistler 606 pressure transducers. Unlike in the previous study [3], in the present experiments the rubber displacements, due to its uni-axial strain loading by the incident shock wave, were very small and could not be detected by high-speed shadowgraph photography. Therefore, other means for measuring the rubber's displacement have to be employed. In the first set of experiments the uni-axial strain loading of a 40 × 40 × 100 mm rubber specimen was achieved by placing it inside the shock tube test

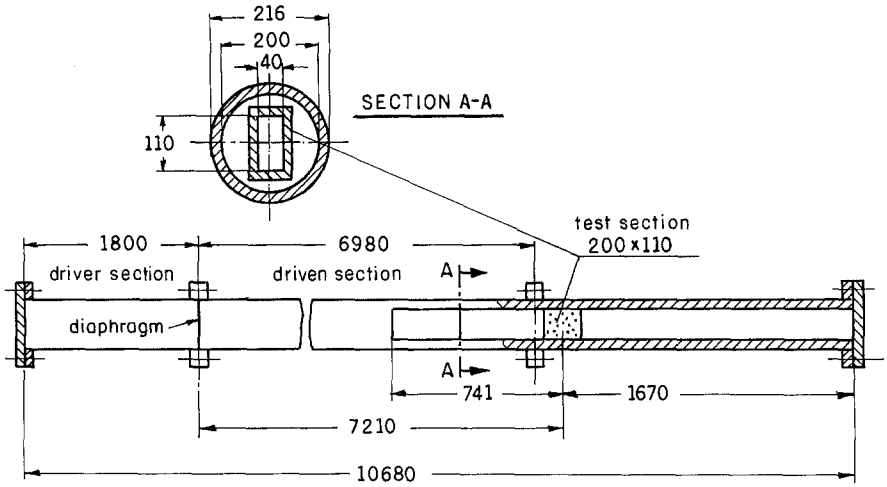

Fig. 2. Schematic description of the EMI shock tube used for studying the head-on collision of a planar shock wave with a rubber rod. All dimensions are in millimeters

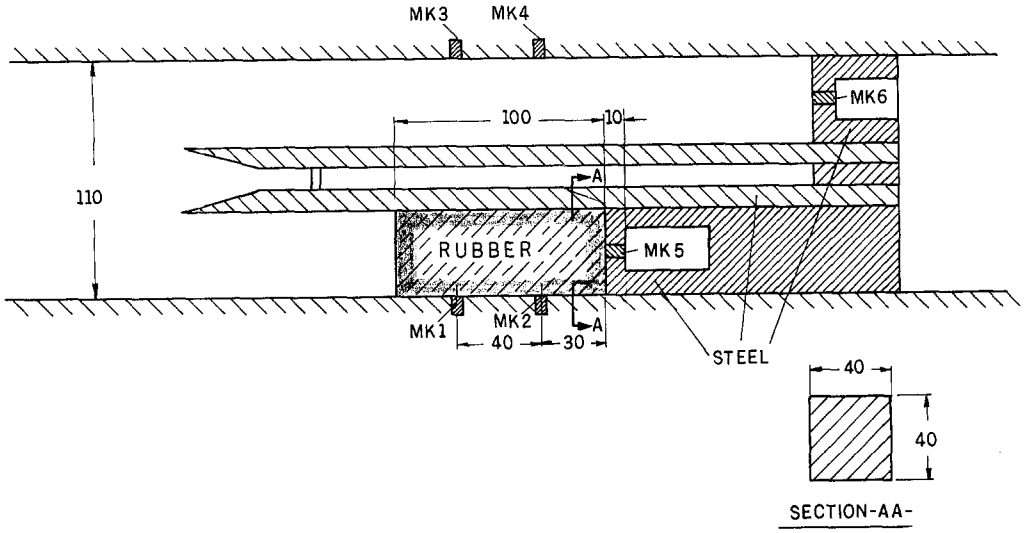

Fig. 3. The rubber rod positioning inside the shock tube test section. MK i ($i = 1, 2, 3, 4, 5, 6$) indicate the location of piezoelectric pressure transducers used for pressure measurements

section as shown in Fig. 3. The chemical composition of the rubber rod used is: natural rubber SMR 100.0 gr, stearine 2.0 gr, zinc oxide 5.0 gr, carbon black Haf 10.0 gr, antioxidant 224b 2.0 gr, sulfur 2.75 gr, CBS 1.00 gr, TMTD 0.10 gr. This composition ensured good elasticity. From static load testing it is found that the rubber specimen's elasticity constant is $G = 9.317$ bar; the rubber Poisson's ratio used in the present computations is 0.495.

Results obtained for this geometry are reported in Ben-Dor et al. [6]. Poor agreement is found between experimentally obtained pressures (stresses) in the rubber and the appropriate numerical simulations, for details see Fig. 3 in Ben-Dor et al. [6]. The main reason for the obtained discrepancy between experimental and numerical results is the use of pressure gauges (MK 1, MK 2 and MK 5 shown in Fig. 2 in [6]) made for pressure measurements in gases to measure pressure (stresses) in the rubber rod.

To confirm the validity of the above explanation regarding the discrepancy between experimental and numerical results obtained for pressures in the rubber rod, a different experimental approach was undertaken. In the new experiments the same rubber specimen that was reported in [6] was used. It was rotated 90 degrees relative to its original position (see Fig. 4). Now the length of the rubber is significantly shorter while the walls bounding it are positioned further away relative to the case reported in [6]. In the new setting a provision is made for an air cushion between the rubber rear surface and the shock tube end-wall. Using this provision results in the Kistler gauges (MK 2, 3, 4 shown in Fig. 4) measuring pressures in the air pocket and not in the rubber as was done before. Such measurements should be accurate, since it is within the specifications of the used gauges. In the first experiment, conducted with the rubber rod setting as shown in Fig. 4, the width of the air cushion was taken as $\delta_1 = 1$ mm. The initial conditions were: $M_S = 1.40$, $P_0 = 0.993$ bar, and $T_0 = 23.3°C$. In such a case pressure transducers MK 2, MK 3, and MK 4 were supposed to read pressures in the gas only. However, as can be seen from the experimental readings shown in Fig. 5, it is quite probable that a momentary contact between the rubber rear surface and the pressure transducers took place; see the pressure peaks in Fig. 5. It should be noted that, while there are discrepancies in the pressure amplitudes between experimental findings and numerical predictions (Fig. 5), the time variations are very similar. The pressure discontinuity in the air pocket, shown in the numerical results at $t \cong 0.9$ ms, is due to the following reason: Once the transmitted compression wave, in the rubber, reaches the rubber rear surface it is reflected back as a rarefaction wave, since this surface is a free surface. At that time the rubber rear surface starts moving into the air cushion and thereby compresses the air there. This

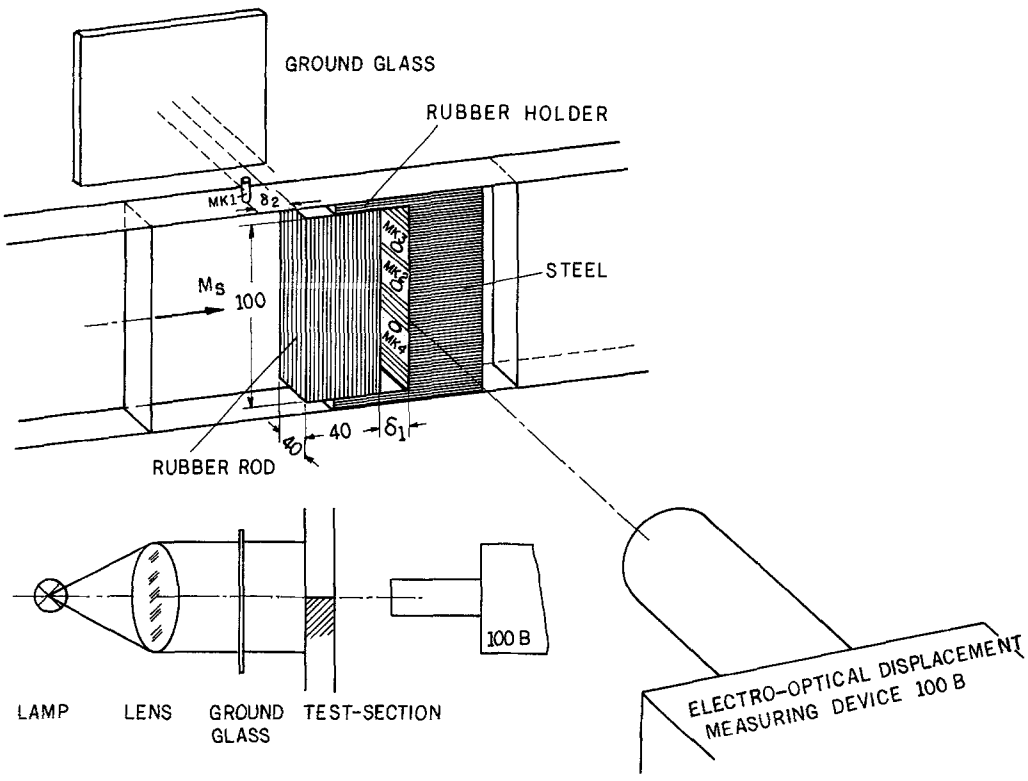

Fig. 4. An alternative positioning of the rubber rod inside the shock tube test section. Also shown is the electro-optical displacement measuring device alignment relative to the shock tube test section. MK i ($i = 1$, 2, 3, 4, 5, 6) are pressure transducers

compression continues as long as the rubber's rear surface moves further into the air cushion. After some time, depending on the size of the air cushion and the strength of the incident shock wave, a situation is reached when the pressure inside the air cushion is equal to the stress prevailing at the rubber rear end (after a few reflections in the rubber). When this happens, the reflected wave from the rubber rear surface is a compression wave. The pressure plateau shown at $0.8 < t < 0.9$ ms (see numerical results in Fig. 5) and the pressure discontinuity at about $t = 0.9$ ms manifest the shift from a reflected rarefaction wave to a reflected compression wave, due to the pressure buildup in the air cushion. At about 1 ms, the rubber rod starts moving away from the air cushion, and the air pressure declines accordingly. As could be expected good agreement exists between experimental (pressures measured by gauge MK 1 in Fig. 4) and numerical results for the static pressure ahead of the rubber specimen, see Fig. 6. The displacement of the rubber specimen frontal surface was too small to be measured from plain photography. To avoid potential contacts between the rubber rear surface and the pressure transducers located at the end wall of the air cushion and to enable measurements of the rubber displacement due to its loading by the incident shock wave, the width of the air cushion was extended.

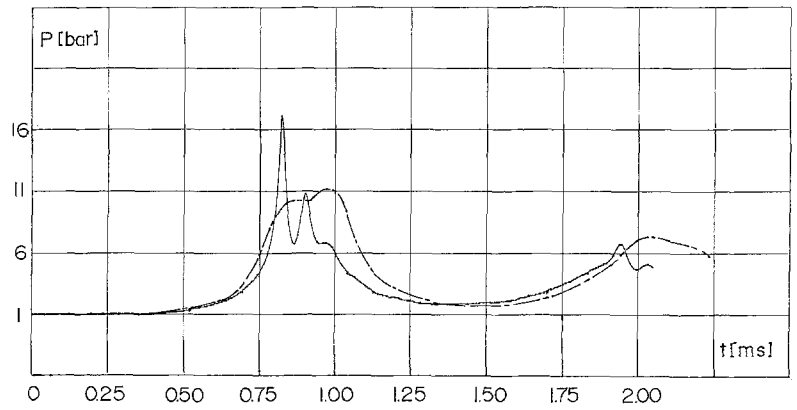

Fig. 5. Pressure variations with time at the location of pressure transducer MK 2 (shown in Fig. 4). Initial conditions are: $\delta_1 = 1$ mm, $\delta_2 = 19$ mm, $P_0 = 0.993$ bar, $T_0 = 23.3$°C, and $M_S = 1.40$. —— Experimental results, — - — numerical results

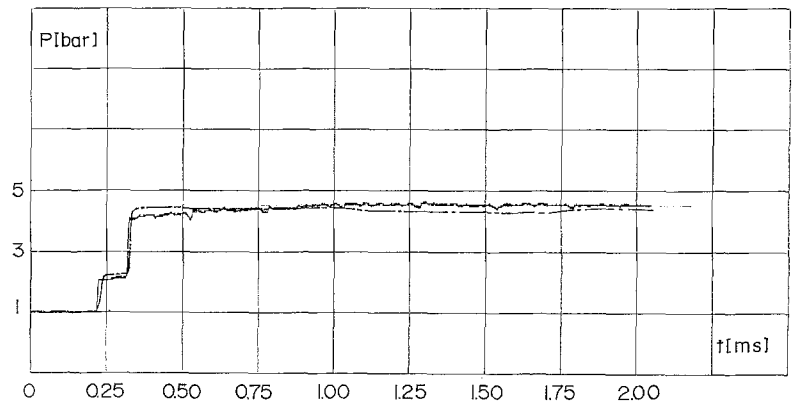

Fig. 6. Pressure variations with time at the location of pressure transducer MK 1 (shown in Fig. 4). Initial conditions are: $\delta_1 = 1$ mm, $\delta_2 = 19$ mm, $P_0 = 0.993$ bar, $T_0 = 23.3$°C, and $M_S = 1.40$. —— Experimental results, — - — numerical results

In the following results, in addition to pressure measurements, the rubber displacement was also recorded using an electro-optical displacement measuring device. Its positioning relative to the shock tube test section is shown in Fig. 4 and a schematic description of the electro-optical unit is given in Fig. 7. This device measures the displacement of a black and white edge in normal direction. The light beam reflected from the black and white edge is focused by a lens into a photo-cathode of an image converter (see Fig. 7). The electron image is reflected within the photo-cathode to a diaphragm having a small hole. At the beginning of each test an adjustment is made to ensure that the measuring beam passes exactly through the hole in the diaphragm. When the black and white lines are displaced, a control circuit displaces the electron image in such a way that a chosen point of the edge always falls on the diaphragm's hole. The current in the control circuit is proportional to the edge displacement; it represents the measuring signal. The rise time of the signal (from 0 to 63%) is less than 1 μs. This optical device can measure displacements to within ± 0.03 mm.

In Fig. 8 experimental and numerical results for static pressure ahead of the rubber specimen (i.e., measured by gauge MK 1 of Fig. 4) are shown. In the present case $M_s = 1.56$, $\delta_1 = 15$ mm, $\delta_2 = 5$ mm, $P_0 = 0.983$ bar, and $T_0 = 21.4°C$. Good agreement exists between the two results

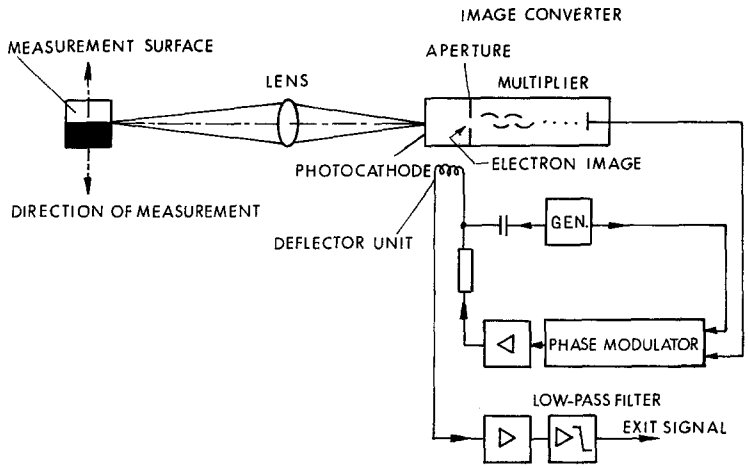

Fig. 7. Schematic illustration of the electro-optical displacement measuring device

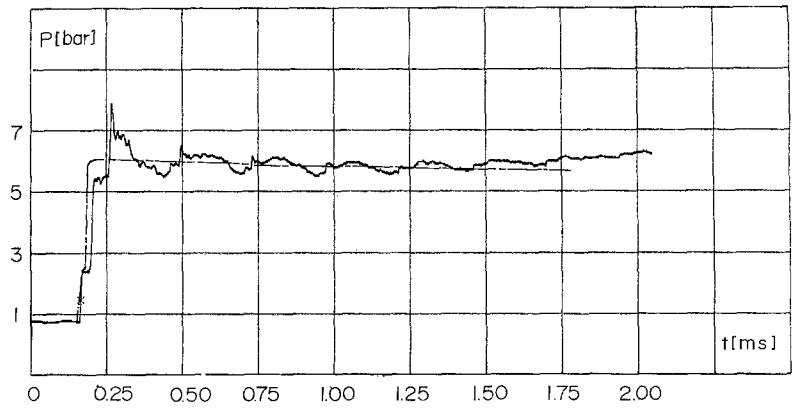

Fig. 8. Pressure variations with time at the location of pressure transducer MK 1 (shown in Fig. 4). Initial conditions are: $\delta_1 = 15$ mm, $\delta_2 = 5$ mm, $P_0 = 0.983$ bar, $T_0 = 21.4°C$, and $M_S = 1.56$. —— Experimental results, – - – numerical results

regarding the pressure jump across the incident shock wave. As for the pressure behind the shock wave reflected from the rubber frontal surface, one can observe that (see Fig. 8): (i) a higher peak is registered experimentally in comparison with the numerical predictions and (ii) the experimental findings suggest the existence of pressure pulses (weak shocks) behind the shock-wave reflected from the rubber's frontal surface. These pressure pulses are the result of shock reflection from the rubber holder in the channel produced between the rubber specimen and the shock tube floor and ceiling (see Fig. 4). This additional flow, in the narrow channel generated between the rubber specimen and the shock tube walls, is not included in our numerical solution. It is, however, quite clear that the average pressure readings at the place where pressure transducer MK 1 is positioned, agree very well with our numerical predictions. The measured and calculated displacements of the rubber rear surface are shown, for the previously mentioned conditions, in Fig. 9. Very good agreement exists between the two results. The displacement measurements reach saturation at $t \cong 1.1$ ms, because for achieving high resolution the measuring signal was additionally increased. At $t \cong 1.1$ ms, in Fig. 9, the upper limit of the transient recorder was reached. The measured and calculated pressures acting on the

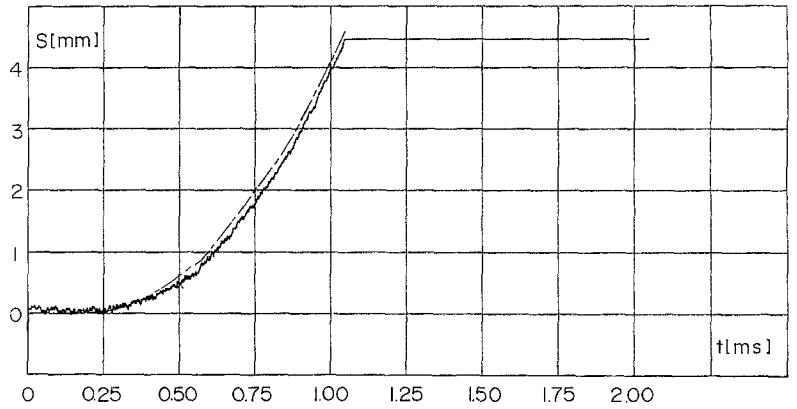

Fig. 9. Displacement of the rubber rod rear surface versus time. Initial conditions are: $\delta_1 = 15$ mm, $S_2 = 5$ mm, $P_0 = 0.983$ bar, $T_0 = 21.4\,^{\circ}C$, and $M_S = 1.56$. —— Experimental results — - — numerical results

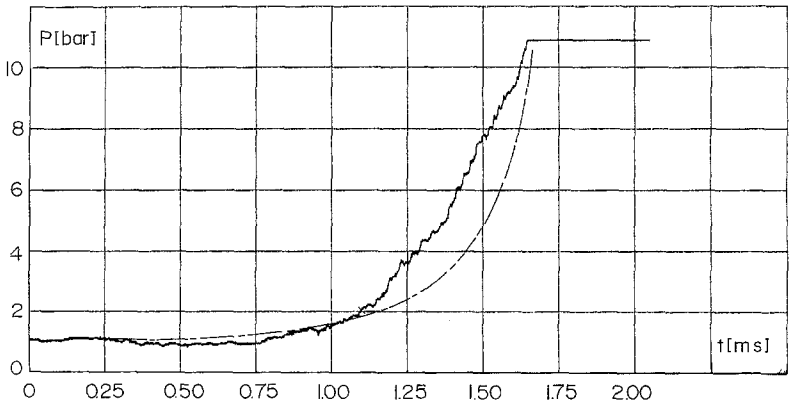

Fig. 10. Pressure variations with time at the location of pressure transducer MK 2 (shown in Fig. 4). Initial conditions are: $\delta_1 = 15$ mm, $\delta_2 = 5$ mm, $P_0 = 0.983$ bar, $T_0 = 21.4\,^{\circ}C$, and $M_S = 1.56$. —— Experimental results, — - — numerical results

steel wall of the air cushion (gauge MK 2, in Fig. 4) are shown in Fig. 10 for the conditions specified previously. The measurements reach saturation at $t \cong 1.62$ ms due to the reason just explained. It is apparent from Fig. 10 that good agreement exists between experimental and numerical results. The agreement is definitely superior to that reported previously (see [6]).

Another set of results is shown in Figs. 11–13. They were obtained for $M_S = 1.54$, $P_0 = 0.99$ bar, $T_0 = 22.8°C$, $\delta_1 = 5$ mm, and $\delta_2 = 15$ mm. It is apparent from Fig. 11 that a very good agreement exists between the measured and calculated pressures ahead of the rubber (pressure gauge MK 1 in Fig. 4). The experimental and numerical results for the displacement of the rubber rear surface are shown in Fig. 12. Again a very good agreement is found between the two results, up to the point where the recorder reading the experimental data reaches saturation. A comparison between numerical and experimental results for the pressure in the air cushion, where pressure gauge MK 2 is placed, is shown in Fig. 13. A good agreement is found between the two results. For all the numerical results shown so far, a friction coefficient of $\mu = 0.04$ is used. Based upon the agreement between the two sets of results shown in Figs. 8 through 13, it can be stated with confidence that the proposed physical model and its numerical simulation describe

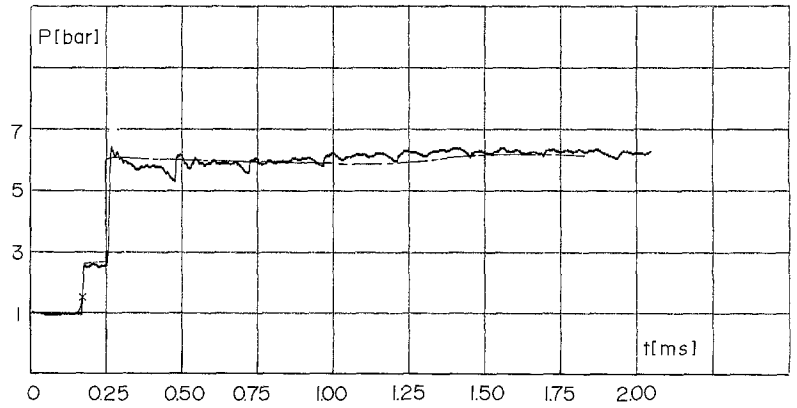

Fig. 11. Pressure variations with time at the location of pressure transducer MK 1 (shown in Fig. 4). Initial conditions are: $\delta_1 = 5$ mm, $\delta_2 = 15$ mm, $P_0 = 0.99$ bar, $T_0 = 22.8°C$, and $M_S = 1.54$. —— Experimental results, – – – numerical results

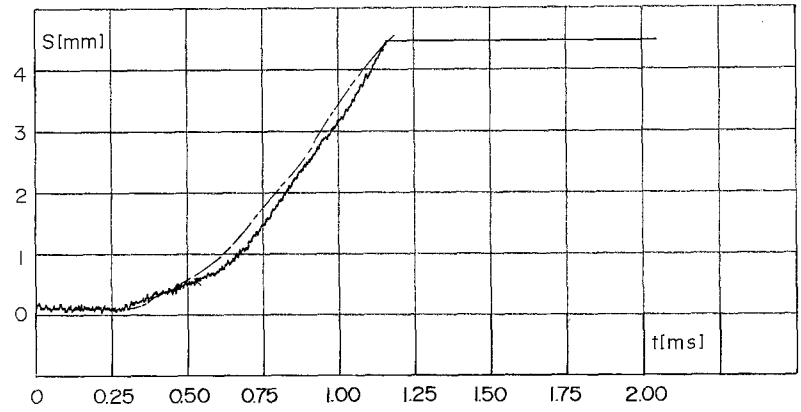

Fig. 12. Displacement of the rubber rod rear surface versus time. Initial conditions are: $\delta_1 = 5$ mm, $\delta_2 = 15$ mm, $P_0 = 0.99$ bar, $T_0 = 22.8°C$, and $M_S = 1.54$. —— Experimental results, – – – numerical results

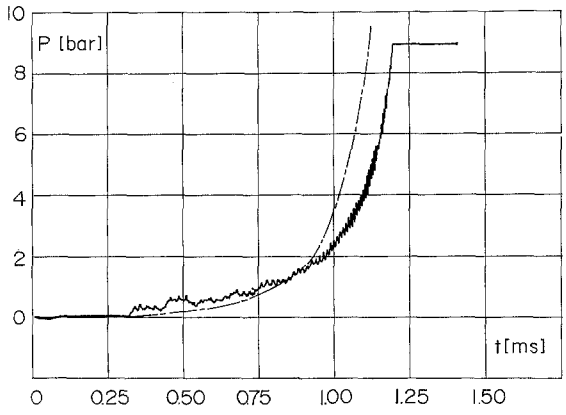

Fig. 13. Pressure variations with time at the location of pressure transducer MK 2 (shown in Fig. 4). Initial condition are: $\delta_1 = 5$ mm, $\delta_2 = 15$ mm, $P_0 = 0.99$ bar, $T_0 = 22.8°C$, and $M_S = 1.54$. —— Experimental results, – – – numerical results

the uni-axial strain loading case satisfactorily. To assess the role played by friction developed between the rubber rod and the shock tube walls, this physical model is simulated numerically for three different friction coefficients, i.e., $\mu = 0$, 0.04, and 0.09. All cases are simulated for the geometry shown in Fig. 3, $M_S = 1.507$, $P_0 = 0.983$ bar, and $T_0 = 21.2°C$. For the rubber we take $G = 9.317$ bar, $\varrho_{r_0} = 1.007$ g/cm^3, and $\nu = 0.495$. The obtained results for pressures in the gas and in the rubber are shown in Fig. 14. At time $t = 0$, marked as line No. 1 in Fig. 14, the incident shock wave is shown prior to its head-on collision with the rubber rod. The gas ahead of the shock wave and the rubber specimen are still experiencing the initial pressure, i.e., $P_0 = 0.983$ bar. 76.1 μs later, the lines marked as No. 2 in Fig. 14, show the reflected and the transmitted waves. The one on the left is the shock wave reflected from the rubber frontal surface and the one on the right is the transmitted wave in the rubber. As time progresses both waves propagate further into the gas and into the rubber, respectively. It is apparent from Fig. 14 that the friction force has a significant effect on the strength of the transmitted wave, in the rubber, but not on its propagation velocity. As expected, it has no effect on the reflected shock wave in the gas. For the case in which no friction is included ($\mu = 0$), the strengths of both the reflected and the transmitted waves are unchanged. Introducing friction, we note a clear weakening of the transmitted wave in the rubber. The larger μ is, the smaller is the pressure jump across the wave (see Fig. 14). How changes in μ effect the strength of the transmitted compression wave in the rubber, and its propagation velocity, can be seen in Fig. 15. It is clear from this figure that, while the velocity of the compression wave is independent of μ (the S versus t curve is a straight line for all μ's), the post-wave pressure depends strongly upon μ. The fact that the wave strength changes without any changes in its velocity is an indication that this is a linear wave (compression wave) rather than a shock wave. Further discussion of this aspect is given below. The strong damping effect of the friction force which develops between the rubber rod and the walls surrounding it is also shown in Figs. 16 and 17. In these figures the pressures prevailing at the location of pressure transducers MK 2 and MK 5 (of Fig. 3) are calculated for three different friction coefficients, i.e., $\mu = 0$, 0.04, and 0.09. In Fig. 16 the pressure at the station where gauge MK 2 is located, is shown as a function of time. In the ideal case of no-friction ($\mu = 0$) the wave motion in the rubber is cyclic due to the absence of a damping mechanism. Once friction is introduced the cyclic wave motion is destroyed. For $\mu = 0.04$, the first pressure cycle, although reduced in strength, is clearly visible. Hence, the pressure jump across the transmitted compression wave in the rubber followed by a further jump across the reflected compression wave from the rubber rod rear surface, and the pressure reduction across the rarefaction wave reflected first from the rubber rod frontal surface and thereafter from its rear surface, are clearly visible in Fig. 16. A further increase in the friction coefficient (to $\mu = 0.09$) results in a dramatic damping; now only the pressure jump across the

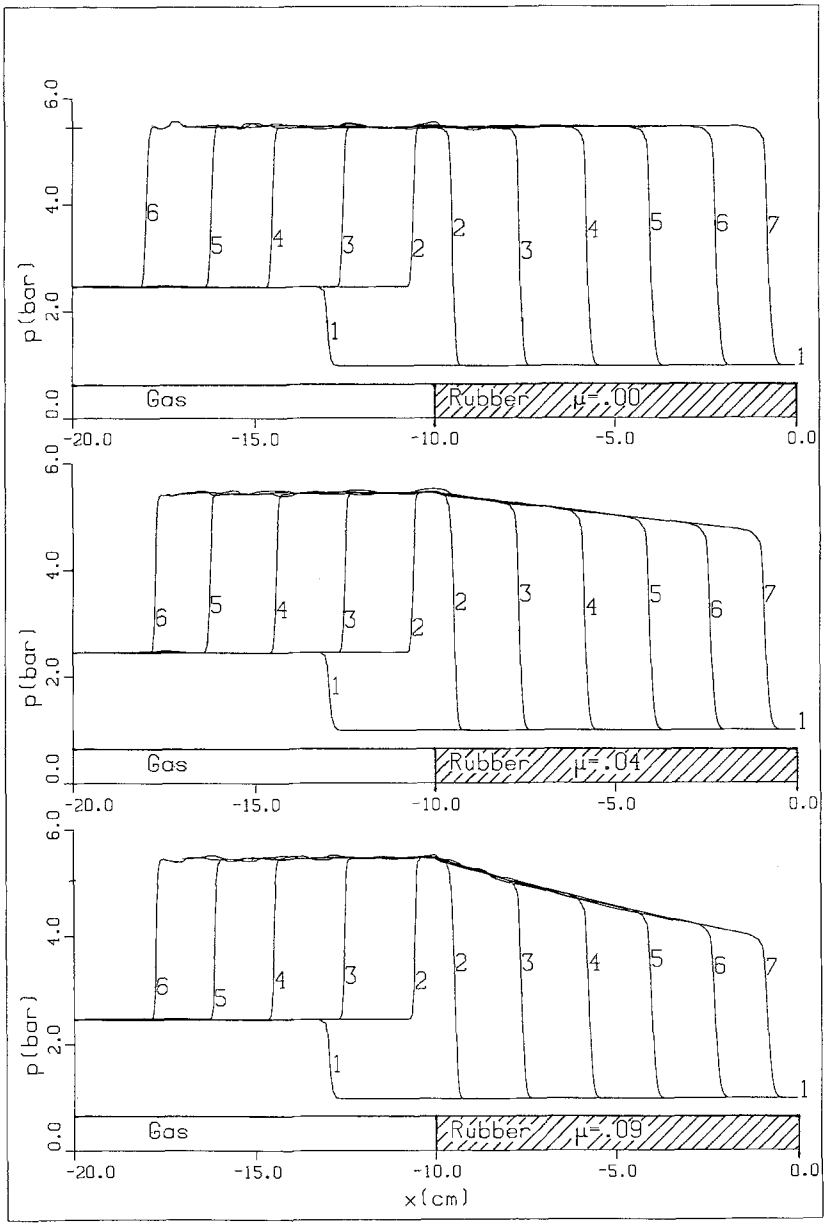

Fig. 14. Numerical results showing the shock waves in the air and the compression waves in the rubber rod at different times

No.	1	2	3	4	5	6	7
time (μs)	0	76.1	136.7	197.3	255.2	311.9	359.7

Initial conditions are: $P_0 = 0.983$ bar, $T_0 = 21.2°C$ and $M_S = 1.507$, $G = 9.317$ bar, $\nu = 0.495$, $\varrho_{r_0} = 1.007$ g/cm^3

incident compression wave and across its reflection from the rubber rod rear surface are noticed. Thereafter a uniform, constant pressure prevails. Similar behavior is experienced at the rubber rear surface, where it is attached to a rigid wall (see Fig. 17). Now ($\mu = 0.09$) only one pressure jump is noticed; namely that existing behind the reflected compression wave from the rubber's surface. As already shown before, the larger μ is, the smaller is the pressure (stress) in the rubber.

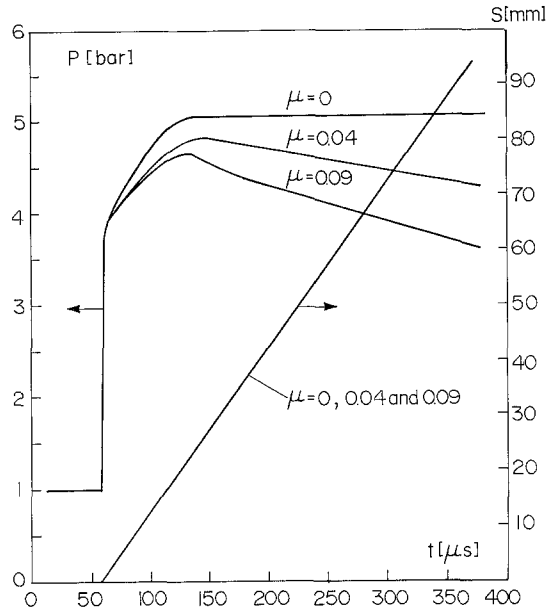

Fig. 15. Numerical results for pressures developed in the rubber, due to the compression wave, and the displacement of its frontal surface for different friction coefficients. Initial conditions as in Fig. 14

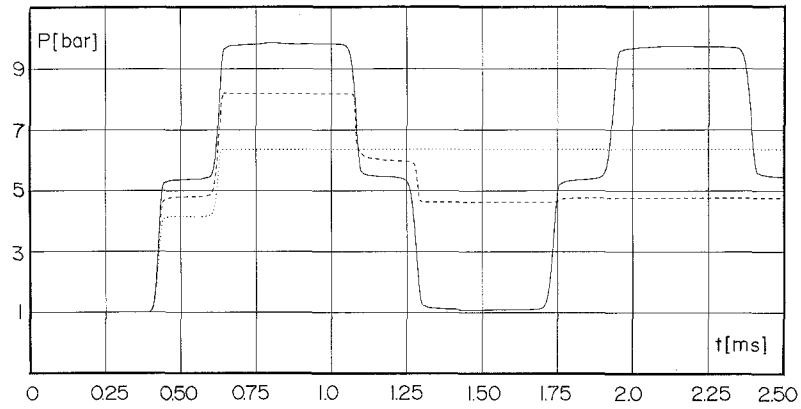

Fig. 16. Numerical results for pressure variation in a rubber rod positioned as shown in Fig. 3. The pressure is calculated at the position of pressure transducer MK 2 (in Fig. 3). Initial conditions as in Fig. 14 [—— $\mu = 0$, — — — $\mu = 0.04$, ... $\mu = 0.09$]

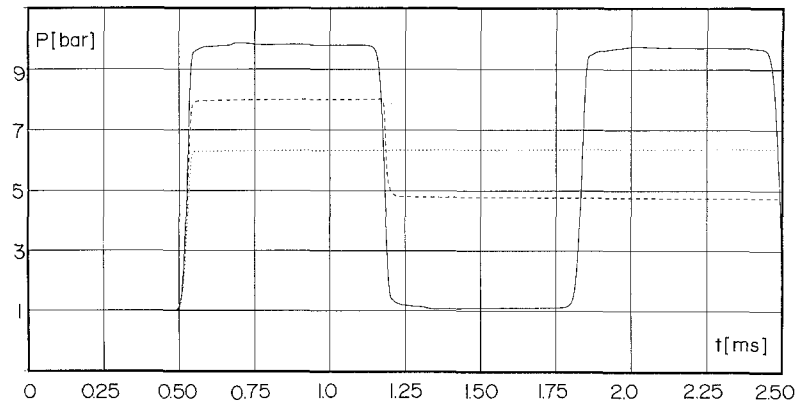

Fig. 17. Numerical results for pressure variation in a rubber rod positioned as shown in Fig. 3. The pressure is calculated at the position of pressure transducer MK 5 (in Fig. 3). Initial conditions as in Fig. 14 [—— $\mu = 0$, — — — $\mu = 0.04$, ... $\mu = 0.09$]

Thus, the friction presence causes significant reduction in the pressure (stress) developed in the rubber rod and changes the wave pattern by damping.

It should be noted here that it is not simple to determine the appropriate friction coefficient under conditions of the present experiments, i.e., for an extremely fast loading. The value of $\mu = 0.04$ is chosen due to the good agreement obtained between experimental and numerical results when this value is used. It is also shown that changes in μ have a significant effect on the obtained numerical results.

As is noted in [3] compression waves do not coalesce to a shock wave for the uni-axial strain loading case. Therefore, for such a loading, only compression waves exist and they propagate with the speed of sound (elastic longitudinal wave). It is also noted there that the highest speed of sound (compressive wave) is encountered in the uni-axial strain loading case. The present numerical results (e.g., those shown in Figs. 14 through 17) indicate that the waves in the rubber propagate with a constant velocity, in the present case it is 305.2 m/s. The rubber particle velocity is significantly smaller, in the present case it is 1.46 m/s only. It is possible to calculate these two velocities analytically, directly from the conservation and constitutive equations. This computation is worth conducting, since it may serve as a further verification of the numerical scheme used.

Consider an incident shock wave (I.S.W.) in the gas moving to the right (see Fig. 18 a), towards a plane AB separating gas and rubber. This shock wave is partially reflected back into the gas, and partially transmitted into the rubber. First, consider a rubber element ABA'B' shown in Fig. 18 b. The prevailing conditions at AB and A'B' are shown in Fig. 18 b, where σ_x is the sress generated in the rubber by the transmitted compression wave (T.C.W.). D is the speed of propagation of the compressive wave in the rubber. Ahead of the compression wave in the rubber ambient conditions exist. u_p is the particle velocity induced by the compression wave in the rubber. From the conservation of mass it follows that

$$\varrho_{r_0} D = \varrho_r (D - u_p), \tag{4.1}$$

and from the conservation of momentum we find

$$\varrho_{r_0} D u_p = \sigma_x - P_0, \tag{4.2}$$

where σ_x is positive for compression.

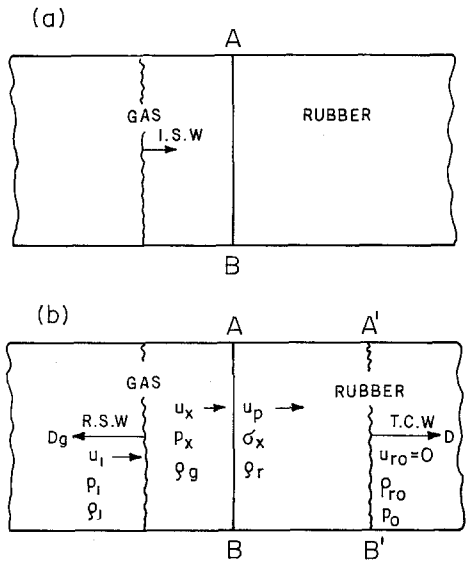

Fig. 18. An illustration showing: in **a**, an incident shock wave in the gas prior to its head-on collision with a rubber rod; in **b**, the reflected shock wave in the gas and the transmitted compression wave in the rubber shortly after the collision

Combining Eqs. (4.1) and (4.2) we obtain

$$\varrho_r u_p(D - u_p) = \sigma_x - P_0, \tag{4.3}$$

or

$$D = u_p + \frac{\sigma_x - P_0}{\varrho_r u_p}. \tag{4.4}$$

Alternatively, from Eq. (4.1) it follows

$$D = \frac{\varrho_r u_p}{\varrho_r - \varrho_{r_0}}. \tag{4.5}$$

From Eqs. (4.4) and (4.5) we have

$$\frac{\varrho_{r_0}}{\varrho_r} = 1 - \frac{\varrho_{r_0} u_p^2}{\sigma_x - P_0}. \tag{4.6}$$

Equation (4.6) relates the rubber densities and pressure (stress) to its particle velocity. In order to assess the rubber particle velocity, an additional, constitutive equation is needed, i.e., the rubber's stress-strain relation. For an uni-axial strain loading case we have

$$\sigma_x = \tilde{E}(1 - \lambda_x) + P_0, \tag{4.7}$$

where $\tilde{E} \equiv E(1 - \nu)/(1 - \nu - 2\nu^2)$. The rubber's non-dimensional extension ratio λ_x is $\lambda_x = \Delta S/\Delta S_0 = \varrho_{r_0}/\varrho_r$ so that Eq. (4.7) can be rewritten as

$$\sigma_x = \tilde{E}\left(1 - \frac{\varrho_{r_0}}{\varrho_r}\right) + P_0. \tag{4.8}$$

Substituting ϱ_{r_0}/ϱ_r from Eq. (4.6) into Eq. (4.8), we obtain

$$u_p = \frac{\sigma_x - P_0}{\sqrt{\varrho_{r_0}\tilde{E}}}. \tag{4.9}$$

Equation (4.9) relates the particle velocity induced by the incident elastic compression wave to the stress intensity σ_x. For the reflected shock wave (R.S.W.) in the gas, a similar (u_p, P) relation can be obtained. It is known from gasdynamics (see Eq. (20) on page 67 in [2]) that:

$$u_x = u_1 - \frac{P_x - P_1}{\sqrt{\frac{\gamma + 1}{2}\varrho_1\left(P_x + \frac{\gamma - 1}{\gamma + 1}P_1\right)}}. \tag{4.10}$$

For the nomenclature used in Eq. (4.10) see Fig. 18 b. The particle velocity induced by the compression wave transmitted through the rubber and the gas velocity behind the reflected shock wave (in the gaseous phase) can be found from Eqs. (4.9) and (4.10) using the following interface conditions:

(i) The forces acting on plane AB (Fig. 18 b) due to the gas pressure and by the rubber stress are equal.

(ii) At plane AB the particle velocity of the rubber is equal to that of the gas.

For the initial conditions used to obtain the results shown in Figs. 14 to 17 ($M_s = 1.507$, $P_0 = 0.983$ bar, $T_0 = 22.2\,^\circ$C, $G = 9.317$ bar, $\nu = 0.495$, $\varrho_{r_0} = 1.007$ g/cm^3), $u_p = 1.467$ m/s;

which is almost identical with the numerical result $u_{p,num} = 1.457\,5$ m/s. Once u_p is known, D can easily be calculated from Eq. (4.1) to yield $D = 305.69$ m/s. Again, we observe a very good agreement with the numerical result $D = 305.2$ m/s.

5 Conclusions

A physical model capable of describing the head-on collision of a planar shock wave with a rubber rod, which results in a uni-axial strain loading, is proposed. This model includes the rubber's compressibility and the friction force developed between the rubber contact areas with its surrounding walls. The proposed physical model is simulated numerically. The good agreement between the numerical and experimental results confirms the reliability of the proposed model and the accuracy of the numerical scheme used for its simulation. Additional support to the accuracy of the present numerical simulation is obtained by comparing the analytical and the numerical results for the velocity of the compression wave in the rubber, and the rubber's particle velocity. It is demonstrated that the analytical and numerical values for these velocities are almost identical.

It follows from the present experimental and numerical studies that:

(a) Friction forces play an important role in the present rubber loading due to its head-on collision with a planar shock wave.

(b) The higher is the friction coefficient, the stronger is the wave damping in the rubber.

(c) In a uni-axial strain loading only compression and/or rarefaction waves exist in the rubber rod but no shock waves. Waves propagate with constant velocity, independent of the friction coefficient and of the intensity of the colliding shock wave.

Acknowledgment

This research was supported by a grant from the German-Israeli Foundation for Scientific Research and Development. Its financial support is acknowledged.

References

[1] Courant, R., Friedrichs, K. O.: Supersonic flow and shock waves. New York: Interscience Publications 1948.

[2] Glass, I. I., Hall, J. G.: Shock tubes. In: Handbook of supersonic aerodynamics § 18 (Penn, S. L., ed.) NAVORD Rep. 1488 (Vol. 6) Bureau of Naval Weapon Publication 1959.

[3] Mazor, G., Igra, O., Ben-Dor, G., Mond, M., Reichenbach, H.: Head-on collision of normal shock waves with a rubber-supported wall. Phil. Trans. R. Soc. London. Ser-A **338,** 237–269 (1992).

[4] Landschhoff, R.: A numerical method for treating fluid flow in the presence of shocks. LASL Report No. LA-1930, Los Alamos, New Mexico, 1955.

[5] von-Neumann, J., Richtmeyer, R. D.: A method for the numerical calculations of hydrodynamic shocks. J. Appl. Phys. **21,** 232–233 (1950).

[6] Ben-Dor, G., Mazor, G., Mond, M., Igra, O., Heilig, W., Reichenbach, H.: Reflection of planar shock waves from rubber walls: uniaxial strain case. AIAA J. **31,** 2184–2186 (1993).

Authors' addresses: Prof. O. Igra, Prof. G. Ben-Dor and Dr. L. Wang, The Pearlston Center for Aeronautical Studies, Department of Mechanical Engineering, Ben-Gurion University of the Negev, Beer Sheva 84105 Israel; Dr. H. Reichenbach and Dr. W. Heilig, Ernst Mach Institute, Freiburg, Germany